



Size effect and order–disorder phase transition in MgAl_2O_4 : synthesized by co-precipitation method

C. Jagadeeshwaran¹ · K. Madhan¹ · R. Murugaraj¹

Received: 24 July 2018 / Accepted: 5 September 2018 / Published online: 10 September 2018
© Springer Science+Business Media, LLC, part of Springer Nature 2018

Abstract

We report on the size effect and order–disorder phase transitions in MgAl_2O_4 system synthesized by chemical co-precipitation method. The prepared samples were sintered at various temperatures (in steps of 200 °C). Initially, the order–disorder phase evolution of the cubic spinel aluminates were analyzed by powder X-ray diffraction and UV-absorbance spectral analysis. The optical band gap was calculated from UV–DRS absorbance spectra. Also, the grain size of the sintered aluminates was calculated by high resolution scanning electron microscopy through surface morphological image analysis and discussed. Moreover, the particle size was calculated by using transmission electron microscopy. The stretching and bending mode of tetrahedral and octahedral coordinates for vibration modes of cations were studied through Fourier transform infrared spectral analysis. In addition, the cation distributions in the prepared samples were carried out by solid-state nuclear magnetic resonance spectroscopic measurement and analyses. The frequency dispersive behavior of dielectric constant was analyzed at room temperature for the synthesized samples using impedance analyzer. The observed results are discussed and reported.

1 Introduction

The spinel aluminates system with general formula XAl_2O_4 (where $X = \text{Zn, Mg, Ni}$ and Co) form of rich ceramic materials and has own properties like high melting point, high mechanical strength at different temperatures, thermal shock resistance, excellent optical properties, and a low dielectric constant, etc. [1–4]. In particular, the magnesium aluminate (MgAl_2O_4) is one of the most attractive spinel oxide materials for device applications. In view of the fact that, it's remarkable support [5], and its possible application in the field of insulating dielectric and humidity sensor [6, 7], as a refractory materials, chemical catalysis and integrate electronic circuits [8–10]. In the recent years, there are different routes employed for the synthesis of aluminates system, in particular for MgAl_2O_4 system, such as modified sol–gel [5], flash pyrolysis route [11], mechano-chemical milling [12], oxide one pot synthesis [7], conventional solid-state reactions, microwave assisted solid-state reactions [13], etc. In particular, the aluminate system which synthesized through low temperature techniques shows a high degree

of chemical homogeneity and better control of stoichiometric, when compared with the other conventional techniques. Mostly, all these types of synthesis routes at low temperature results in the amorphous phase of the magnesium aluminates sample. Among these synthesis routes, the chemical co-precipitation method evolved the single crystalline phase at low temperature. Apart from these, the review of literature shows a good number of reports on the chemical induced phase evolution of the MgAl_2O_4 system as a function of calcination temperature [14]. Also, the order and disordered phase of spinel structure has been reported by very few workers through irradiation-induced structural change of MgAl_2O_4 system [15, 16].

The aluminate structure of MgAl_2O_4 contains 2–3 spinel co-ordinate system. The 2^+ refer to minority of divalent atom is Mg site and 3^+ refer to majority of trivalent atom is Al site. The cation co-ordinates are only 24 sites (8 tetrahedral of A-site and 16 octahedral of B-site) and anion between 96 interstices (64 tetrahedral and 32 octahedral) sites [17]. The cation distributions in the spinel structure are decided at octahedral and tetrahedral site positions through the ionic radius and electro-negativity of cations [18]. The stoichiometric ratio of Mg-aluminate, the defects correspond to anti-site pairs, where the cations exchange sites of (tetrahedral and octahedral pairs). In order to lower the magnitude of anti-site defects, which is related to an

✉ R. Murugaraj
r.murugaraj@gmail.com

¹ Department of Physics, Anna University, MIT Campus, Chennai 600 044, India

intrinsic defect processes. But, the anti-site disorder dominates the defect chemistry of this system [19]. The cation in the sites provides the order–disorder phase and described by the degree of inversion (j). The degree of anti-site cation disorder is provided by the inversion parameter, j , defined as $(Mg_{1-j} Al_j) [Mg_j Al_{2-j}] O_4$, where the curved brackets refers to a tetrahedral site and the square brackets refers to the octahedral sites. In other words, j represents the fraction of tetrahedral sites occupied by trivalent cations. The inversion parameters for normal, statistically random, and inverse spinel structures are 0, 2/3, and 1, as reported in the literature [19, 20]. The Mg-aluminate here refer to partially inverse spinel structure because of the ordered–disorder phase variation is observed for different sintering effect. Up-to-date all literatures reviews on the synthetic $MgAl_2O_4$ system shows only very few reports on the disorder–order phase variation.

In the present work, $MgAl_2O_4$ has been prepared by chemical co-precipitation method at ambient temperature. The results suggest that the size effect dependence upon disordered to ordered phase variation were observed. In the literature, the order–disorder phase has been correlated through the studies by X-ray diffraction (XRD) pattern and UV-absorbance spectra. Therefore, the aim of the present work to synthesis the magnesium aluminate system through co-precipitations method. The prepared samples were sintered at different temperatures and studied the disorder to order phase transitions as induced by sintering effect. The structural characterization of the samples were analyzed through XRD technique, NMR spectral analysis, and correlated with SEM and TEM analysis. The optical properties were characterized by UV–DRS method to ascertain the order–disorder phase transition in the sintered samples. Also, we have attempted to study the presence of order–disorder phases in the magnesium aluminate system through the dielectric properties at the room temperature. The observed results were discussed and reported.

2 Experimental

The starting raw materials are analytical reagent grade nitrates of Magnesium ($Mg(NO_3)_2 \cdot 6H_2O$) and Aluminum ($Al(NO_3)_3 \cdot 9H_2O$) are taken in the corresponding stoichiometric ratio and dissolved in double distilled water. The mixture solution was constant stirred with a magnetic stirrer for more than 1 h. The pH of the mixed solution was maintained at ~ 9 by using required amount of aqueous ammonia. Subsequently, the solution turns into milky white with precipitation and continuously stirred for another 30 min. The precipitated solution was washed and dried in hot oven at $100^\circ C$. Finally, the dried samples were equally divide into three parts and transfer to alumina crucible and sintered in a furnace at three different temperatures, viz., $500^\circ C$, $700^\circ C$

and $900^\circ C$ for 3 h in open atmosphere. Henceforth, the sintered samples at $500^\circ C$, $700^\circ C$ and $900^\circ C$ were labeled as Mg5, Mg7 and Mg9, respectively.

The structural and phase formation of the prepared Magnesium aluminate samples were studied through XRD measurement (Bruker D2 Phaser X-ray diffractometer with $Cu K\alpha$ line with 1.546 \AA) and its analysis. In addition, the solid state nuclear magnetic resonance (SS-NMR) spectra were recorded at room temperature for the prepared samples using ^{27}Al source with a Bruker (AV 400) spectrometer at a spinning rate of 10 kHz. The applied magnetic field of 9.389T (400 MHz) corresponds to a ^{27}Al resonance frequency of 104.17 MHz. The surface morphological images of the prepared samples were carried out by HR-SEM (FEI Quanta FEG 200) for grain size analysis. Transmission electron microscopy (TEM) image of prepared samples were recorded using JEOL JEM 2100F TEM for particle size analysis. The UV–DRS (Varian-5000) optical absorbance spectra of the prepared samples were recorded in the 200–800 nm wavelength regions. The stretching and bending modes of octahedral and tetrahedral coordinates were analyzed by Fourier transform infra red (FT-IR) spectroscopic analysis (Perkin Elmer-2000). The calcined sample was pelleted using hydraulic press and the pellet sample was sintered for 6 h. The electrical measurements were carried out using impedance analyzer (PSM1735 NumetriQ (U.K)) in the frequency range of 100 Hz–1 MHz at room temperature. The observed results are discussed below.

3 Results and discussion

3.1 Powder XRD analysis

Figure 1a shows the powder XRD patterns of Magnesium aluminate samples sintered at three different temperatures (sample code: Mg5, Mg7 and Mg9) are given. The XRD pattern indicates that the formation of single crystalline phase with spinel aluminate structure through a well defined diffraction peaks. Further, the intensity of the peaks are well developed and peak becomes broad to shaper as the sintering temperature increases and it is in agreement with literature reported data [21]. From Fig. 1a, we observed a small amount of aluminum oxide (Al_2O_3) impurity peaks were seen at the low temperature sintered (Mg5 and Mg7) samples. As the calcination temperature increases, the intensity of the impurity peaks were very insignificant. Therefore, we concluded that the appearance of the impurity peaks at low temperature sintered samples (synthesized by co-precipitation method) is due to provoke of mixed $MgO-Al_2O_3$ phases. Review of literature also shows that the phase formation of spinel structure was observed at above $410^\circ C$ and below that temperature the transition phase only exists [22].

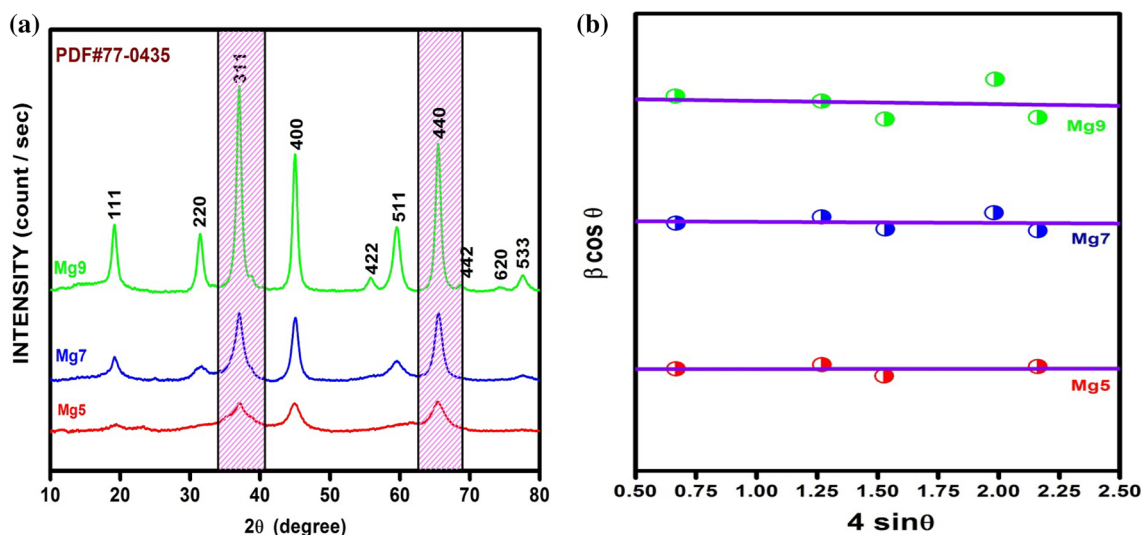


Fig. 1 **a** XRD patterns of MgAl_2O_4 samples sintered at different temperatures. **b** Williamson–Hall plot of MgAl_2O_4 samples sintered at different temperatures

All the diffraction peaks were indexed and compared with JCPDS card no. 77-0435 and well assigned to the cubic system with a majority of space group of Fd-3m (O_h^7): 227 of spinel aluminate structure. The average crystallite size was calculated using Williamson–Hall (W–H) plot as shown in Fig. 1b. The calculated average crystallite sizes are in the order of nano-meter range. The magnitude of micro-strain induced in the lattice is also calculated using Williamson–Hall relation.

$$\beta_{1/2} \cos \theta = \frac{K\lambda}{D} + 4\epsilon \sin \theta \quad (1)$$

where D is the average crystallite size, λ is the monochromatic wavelength of the XRD radiation (1.54056 \AA for $\text{Cu K}\alpha$ line), k is a constant equal to 0.94, $\beta_{1/2}$ is the full width at half-maximum of the intensity peak. In the present case, we utilized the *Voigt function* to get full width at half maximum for a peak position at θ . The lattice parameters were calculated by using following relation

$$f(\theta) = \frac{1}{2} \left(\frac{\cos^2 \theta}{\sin \theta} + \frac{\cos^2 \theta}{\theta} \right) \quad (2)$$

The X-ray density ($\rho_{\text{X-ray}}$) of the sample was calculated using relation [23].

$$\rho_{\text{X-ray}} = \frac{n[M_{\text{Mg}} + 2M_{\text{Al}} + 4M_{\text{O}}]}{V \times N_a} \quad (3)$$

where M is the molecular weight of the sample (viz., Mg, Al and O), V is the volume of the unit cell and N_a is the Avogadro's constant and with the number of unit cells of

cubic spinel system as $n=8$. The calculated values are tabulated in Table 1. From the XRD analysis, we observed that while sintering temperature increases, the intensity of the diffracted peaks also increases that result in the increase in the crystalline nature as well as an increase of the crystallite size. The micro-strain and X-ray density values were decreases and increasing calcined temperature due to the effect of impurity or may be intrinsic defects in the sample. In addition to the above, the observed increase in the magnitude of the lattice parameter could be attributed due the cation distributions at Al^{3+} sites, i.e., due to the distribution of charges either tetrahedral or octahedral sites. In addition, the cation distribution sites of Al^{3+} ion were analyzed and discussed below using solid state NMR spectra analysis.

The several techniques like sol–gel [24], solid state reaction [25] and Pechini [26] methods were used to synthesis normal spinel form not able to observe of order/disorder phases. Even so, very few are discuss about the ordered phase transitions for spinel aluminate structure are the citrate–nitrate (auto-ignition route) [14] and flash pyrolysis route [11]. The low temperature of spinel aluminate structure all the diffraction peaks corresponding to MgAl_2O_4 with order–disorder phase transition was observed shown in Fig. 1a. From Fig. 1a, the Mg5 and Mg7 samples show a high intensity peak at $2\theta = 65.48$ for (4 4 0) plane and for the Mg9 sample the high intensity peak was observed at $2\theta = 37.04$ for (311) plane. In addition, due to particle size increases, the XRD pattern reveals that the phase of spinel structure changes from (dis)ordered to ordered phase [14]. The peaks of high intensity (311) plane were representing the odd reflections and like (400) planes were representing the even

Table 1 Calculated values of lattice parameter, crystalline size, X-ray density, micro-strain, fitted value from UV-absorbance spectra and dielectric properties for Mg5, Mg7 and Mg9 samples

Sample code	Lattice parameter (nm)	Crystalline size from W–H plot (nm)	X-ray density (gm/cm ³)	Micro-strain $\times 10^{-3}$	From UV absorbance spectra		Dielectric constant (ϵ') at 1 KHz	Tan (δ)
					Peak positions (nm)	FWHM (nm)		
Mg5	8.0685	4.5	3.641	5.29	212	51	162	2.4
					275	78		
					367	80		
Mg7	8.0717	8.19	3.634	3.36	201	57	240	3.2
					265	86		
					368	63		
Mg9	8.0783	19.5	3.601	1.84	269	86	67	0.9
					373	41		

reflections. The ordered-disordered phase transitions were compared by degree of orderness through the odd and even peaks intensities. For spinel structure, the degree of orderness can be calculated as:

$$\Sigma I = \frac{I_o}{I_o + I_e} \quad (4)$$

where the intensity peak of odd reflection refer to (I_o) and the peaks of even reflection refer to (I_e). Therefore, from the above an equation, when the particle size increases gradually then the degree of ordered phase also increases. The intensity peaks of supporting odd and even reflection planes were playing a major role for the presence of order–disorder phase present in the sample. The even reflection (222) intensity increases gradually odd reflection (111) also increases, then the intensity of peaks due to disorder spinel remain constant and which may result in the shift of the atom to the interstitial site as reported by Sickafus et al. [15]. The order–disorder phase of higher intensity peaks of (311) and (400) more preferred for order phase calculation on the basis of peak intensity is accurate as reported [15]. Moreover, the higher intensity order phase of (311) and disorder phase of (440) are more contribution to spinel structure of (dis) orderness. The particle size of nanoparticles is more relevant to studies of cation distribution by Sreeja et al. [27]. The cation distribution in the disorder phases of Al^{3+} are present both the tetrahedral and octahedral site due to the vacancy depend upon due to the size (nanoparticles) or as well as the low temperature sintering. The cation distribution of order phases of Al^{3+} move towards to octahedral site from tetrahedral due to the defect phase at high temperature. The cations provoke at high temperature region are toward more stable states of equilibrium position [11]. In this paper, we report on the order–disorder phases transitions in $MgAl_2O_4$ system synthesized through the co-precipitation method at different sintering temperature by tuning the degree of phases.

3.2 NMR analysis

The synthesized spinel aluminates $MgAl_2O_4$ samples were further investigated by ^{27}Al solid state NMR spectroscopy for site exchange effect. The room temperature recorded NMR spectra of the Mg5, Mg7 and Mg9 samples were shown in Fig. 2a. In the literature, the cation distribution of Al^{3+} coordinates in the spinel system at tetrahedral and octahedral site were exchange due to the effect of quadrupole broadening [28]. The octahedral sites were representing the central transition band of quadrupole nucleus, which referred as first and second order quadrupole interaction for single and doublet peaks splitting of quadrupole interactions. As well the satellite transition band and sideband were representing the tetrahedral and octahedral sites [29].

Usually, the Al^{3+} coordinates at tetrahedral position (AlO_4) is denote as (*) and at octahedral site (AlO_6) is denote as (o). In the present work, for $MgAl_2O_4$ system, from the spectra, the peaks were observed around in the range between isotope chemical shift of tetrahedral and octahedral peaks are 48 to 93 ppm and 40 to –40 ppm, respectively. For the comparison purpose, the NMR chemical shift was shown in Fig. 2b for the sintered $MgAl_2O_4$ system. From Fig. 2b, we observed that while increasing the sintering temperature, the observed chemical shift moves toward the negative side. Thus, the tetrahedral and octahedral Al^{3+} peaks were slightly shifted respectively, as 73.29 ppm and 14.15 ppm for Mg5, 74.57 ppm and 14.5 ppm for Mg7 and 73.84 ppm and 11.95 for Mg9. Thus, we concluded that the Mg5 and Mg7 show the first order quadrupole interaction and with octahedral (AlO_6) sideband is observed. But, for Mg9 sample, we observed a second order quadrupole interaction peaks and with tetrahedral (AlO_4) and the octahedral (AlO_6) sideband in the same region and well matched with literature reported data [30].

However, the review of literature shows that the $MgAl_2O_4$ is partially inverse spinel aluminate structure. The general

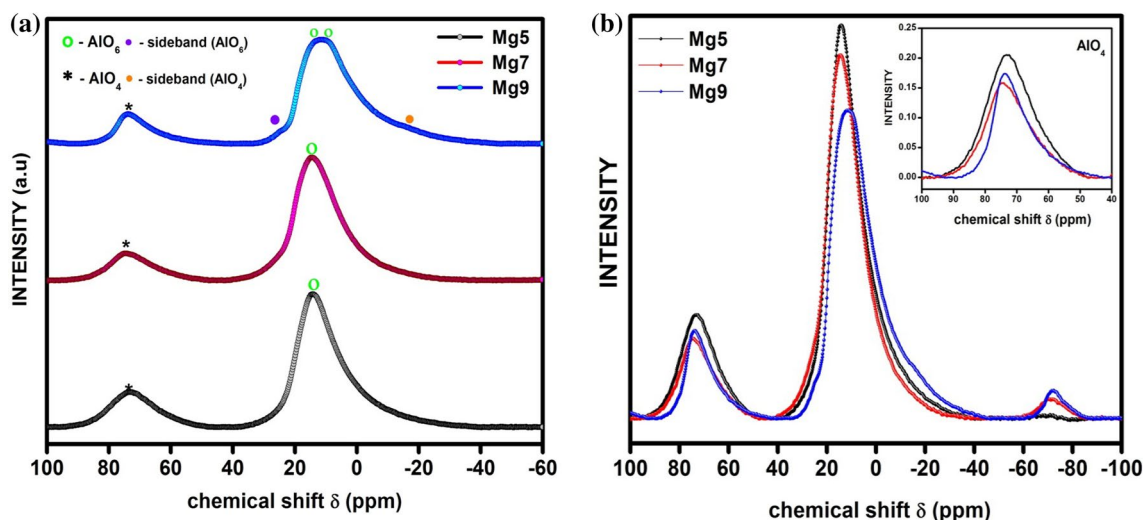


Fig. 2 **a** Room temperature NMR spectra of MgAl_2O_4 samples sintered at different temperatures. **b** Peak shifts in the NMR spectra of MgAl_2O_4 samples sintered at different temperatures

formula of $(\text{Mg}_{1-\delta}\text{Al}_\delta)^{[\text{tetra}]}\text{(Al}_{2-\delta}\text{Mg}_\delta)^{[\text{octa}]}\text{O}_4$. The 2–3 spinel structure of inverse parameter or the degree of inversion ‘ δ ’ was calculated from the ratio of corresponding intensity peaks of Al coordinate in the octahedral (AlO_6) site and in the tetrahedral (AlO_4) site through

$$\delta = \frac{2I_{\text{tetra}}}{I_{\text{tetra}} + I_{\text{octa}}} \quad (5)$$

where I_{tetra} and I_{octa} is intensity of tetrahedral and octahedral peaks were observed from NMR plot. From the recorded NMR spectra, the degrees of inversion (δ) have been found for different temperature sintered samples. The cation distribution was calculated using, the degrees of inversion (δ) relation. The cation distributions of Mg9 and Mg7 samples were reported [31, 32]. Such as we reported the low sintering temperature of cation distributions of Mg5 and the following intensity ratio’s parameter are Mg9 is $(\text{Mg}_{0.57}\text{Al}_{0.43})^{[\text{tetra}]}\text{(Al}_{1.57}\text{Mg}_{0.43})^{[\text{octa}]}\text{O}_4$, $(\text{Mg}_{0.66}\text{Al}_{0.34})^{[\text{tetra}]}\text{(Al}_{1.66}\text{Mg}_{0.34})^{[\text{octa}]}\text{O}_4$ for Mg7 and $(\text{Mg}_{0.59}\text{Al}_{0.41})^{[\text{tetra}]}\text{(Al}_{1.59}\text{Mg}_{0.41})^{[\text{octa}]}\text{O}_4$ for Mg5. On increasing the sintering temperature, the intensity peak ratio of tetrahedral and octahedral site gradually increases for Mg5 and Mg7 and the intensity ratio of Mg9 suddenly decreases. This may be attributed to the structural phase transition from disordered to ordered phase due to sintering effect. This implies that the cation order in MgAl_2O_4 spinel depends upon the sintering effect. This behavior is in good agreement with the XRD data analysis.

3.3 Optical properties

Figure 3a shows the absorbance spectrum for Mg5, Mg7 and Mg9 samples using diffuse reflection spectroscopic

technique at room temperature. All the absorbance spectra were fitted using a Gaussian function [33]. From the fitted data, we calculated the peak position, peak intensity and its full width at half maxima of the corresponding peaks as shown in Fig. 3a. The calculated fitted data are reported in Table 1. The peaks associated with the Mg^{2+} ions were represented by the green dotted line and the two different peaks associated with Al^{3+} ions were represented by the pink and blue dotted lines. On increasing the particle size i.e., on increasing the sintering temperature of MgAl_2O_4 , particularly the peaks of Al^{3+} changes due to disordered to ordered phase as observed in Fig. 3a. In particular, the peak of Al^{3+} was observed at Mg5 and Mg7, which refer to disordered phase and the peak of Al^{3+} were disappeared for Mg9 sample, which referred to an ordered phase. Thus the disappearances of the peak in the UV absorbance spectrum are good in agreement with the results from the XRD pattern. The absorbance peaks of Mg^{2+} and Al^{3+} coordinates get slightly shifted towards the lower wavelength region as the sintering temperature increases.

In the present case, due to sintering effect, the Mg5, Mg7 and Mg9 samples shows three different transition peaks as shown in Fig. 3a. The Al^{3+} coordinate of tetrahedral and octahedral (both) sites are present and while comparing the peaks associated with tetrahedral site of Al^{3+} are more dominate to peaks of octahedral sites at the particle size region of Mg5 and Mg7. The tetrahedral peaks were negligible at higher particle size region of Mg9 sample. The (Al^{3+}) tetrahedral coordinates shows a hump like peak as observed at around 210 nm and the absorption peaks observed around between 250 and 285 nm and at 265 nm were octahedral coordinates of (Al^{3+}) [34, 35]. In addition, the F^+ center vacancies of Mg^{2+} were created due to heating (sintering)

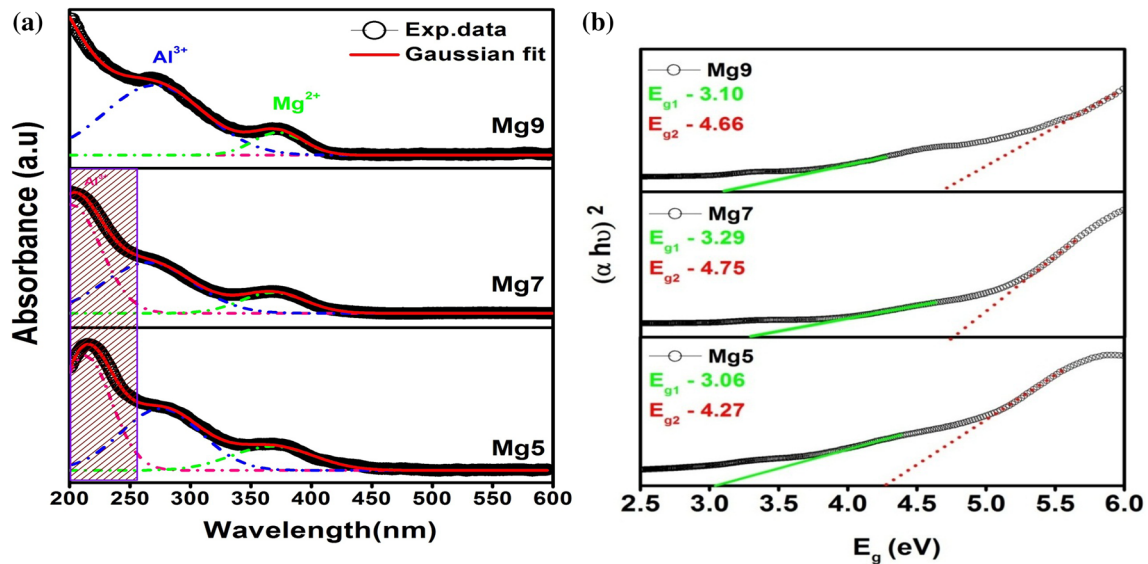


Fig. 3 **a** Room temperature UV-absorbance spectra with Gaussian fit for MgAl_2O_4 samples sintered at different temperatures. **b** Tauc plot of UV-absorbance spectra for MgAl_2O_4 samples sintered at different temperatures

effect of samples as reported [36] and the shoulder peaks observed between 355 and 375 nm were assigned to the tetrahedral coordinates of the Mg^{2+} ion [37].

A very strong absorption peaks were observed around UV region for all the sintered samples. The cut-off wavelength of the absorption peaks for Mg5, Mg7 and Mg9 samples are 373 nm, 366 nm and 368 nm for E_{g1} and 283 nm, 270 nm and 266 nm for E_{g2} , respectively. The band gap energies were calculated from corresponding point of intercept in the wavelength as the cut-off wavelength using

$$E_g = \frac{1240}{\lambda} \quad (6)$$

where the λ is wavelength of absorbed range from the spectrum and E_g is optical band gap energy (eV). The value of simple relation (UV-spectrum) is 3.32, 3.39 and 3.36 (eV) for E_{g1} and 4.38, 4.58 and 4.65 for E_{g2} . The band gap energies were calculated by Tauc plot using

$$(\alpha h\nu)^n = A(h\nu - E_g) \quad (7)$$

where α is the absorption co-efficient constant and frequency dependence take place from the appropriate of UV spectrum, $h\nu$ is the incident photon energy, A is constant depended upon the type of possible transition and n is the power coefficient of allowed transition. If $n = 1/2$ allowed direct band-gap transition and $n = 2$ allowed indirect band-gap transition. The intercept of straight line from the plot between $(\alpha h\nu)^2$ and $h\nu$ (eV) for direct band-gap and the extrapolation linearly position of plot $(\alpha h\nu)^{1/2}$ and $h\nu$ (eV) for indirect band-gap [38]. As the sintering temperature increases, the band-gap also increases [39]. The two absorption band was observed

E_{g1} and E_{g2} . The E_{g1} is inter-band absorption were observed (visible region) of direct and indirect band-gap region. The inter band absorption is only possible if the photon energy exceed the band gap energy E_g . The absorption spectrum therefore shows that a threshold of E_g . The absorption coefficient in the spectra region around E_{g1} is extremely large than the E_{g2} was explained in density of state DOS [40]. The strong absorbance of band gap is E_{g2} (UV region). The inter-band transitions in indirect gap materials involve the absorption or emission of a phonon to converse momentum in process. The indirect absorption is much weaker than direct absorption since it is a second order process [40]. From Fig. 3b, the two band gap region was observed E_{g1} and E_{g2} . The inter-band gap region of E_{g1} was observed in visible region and the strong absorbance of band gap region of E_{g2} was observed in UV region [41]. The UV absorbance region band gap of E_{g2} well matched to reported band gap. Moreover the band that appeared close to the visible light region for each spectrum may be attributed to the O^{2-} and Al^{3+} charge transition due to the excitation of electrons from the valence band of O (2p) to conduction band of Al (3d) [42].

In the present case, the direct band gap energy have been found to be in the range of 3.06, 3.29 and 3.10 (eV) for E_{g1} and 4.27, 4.75 and 4.66 (eV) for E_{g2} [42] and for Indirect band gap energy have been found to be in the range of 2.53, 2.71 and 2.41 (eV) for E_{g1} and 3.12, 3.28 and 3.14 (eV) for E_{g2} is calculated by using the Tauc's plot method. The cut-off wavelength from simple relation is nearly close to direct band-gap value and the indirect band-gap value is less than the direct band-gap value. As a result, the increasing sintering temperature with suddenly increases

and decrease of band gap energy trend by disorder to order phase transition and the slightly shift in absorption edge and widening of the band gap can be explained on the basis of Burstein–Moss shift with size effect dominating role of blue shift of MgAl_2O_4 .

3.4 Functional group analysis

Figure 4 shows the FT-IR spectrum recorded in the range from 400 to 2000 cm^{-1} for the Mg5, Mg7 and Mg9 spinel aluminate system. With the review of literature data four different modes of vibration band were observed and assigned as (ν_1), (ν_2), (ν_3) and (ν_4) and pointed out in Fig. 4 [43]. The oxygen ion bonding as a strong bonding nature and assigned to the high frequency modes (ν_1) and (ν_2), and the metal anion's bonding as weak bonding characteristics and assigned to the lower frequency modes as (ν_3) and (ν_4) with a less sharp peaks as observed.

The stretching and bending vibration mode was observed around 500–700 cm^{-1} and 330–450 cm^{-1} range due to the cations-oxygen octahedral coordinates (AlO_6). However, a tetrahedral coordination (AlO_4) is expected to give stretching modes within the narrow range 700–850 cm^{-1} and bending modes between 250 and 320 cm^{-1} [28, 44]. The vibration mode ranges around 500–700 cm^{-1} due to AlO_6 [11]. The degenerate modes of vibration were also attributed at very lower frequencies [45, 46]. On the other hand, the ordered and disordered phase vibration modes were rarely reported for FTIR spectra [47]. In the disorder phases, the vibration bands for tetrahedral coordinate for stretching mode of AlO_6 were lies around 640 cm^{-1} . Due to the size effect, the

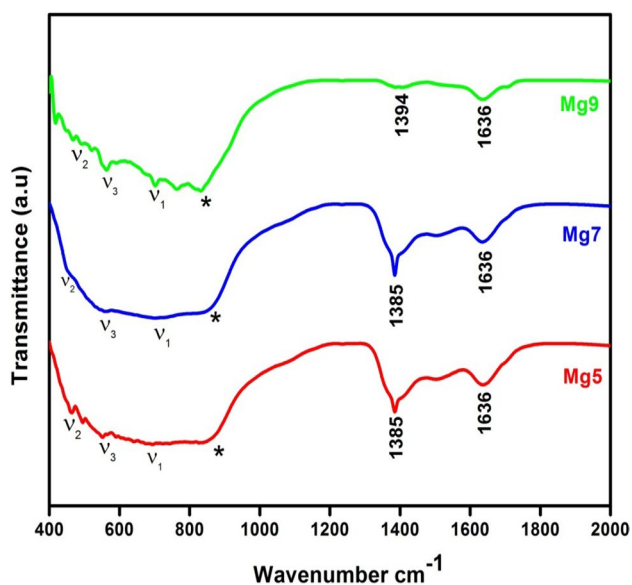


Fig. 4 Function group analysis of FTIR spectra for MgAl_2O_4 samples sintered at different temperatures

vibration bands at 552 and 693 cm^{-1} are assigned to the stretching modes of AlO_6 [48].

For Mg5 and Mg7 samples, with the AlO_4 in a tetrahedral coordinates, the bands at around 560 cm^{-1} are assigned to the stretching modes of AlO_6 and the band observed at 700 cm^{-1} is assigned to the stretching mode of AlO_4 [43]. For the ordered phase of Mg9 sample, the bands of 563 and 520 cm^{-1} are assigned to the stretching modes of AlO_6 . The band observed at 417 cm^{-1} was assigned to the bending mode of AlO_4 [28] and the band observed around at 702 and 764 cm^{-1} was assigned to the stretching mode of AlO_4 . On increasing the temperature, the Mg–O denoted as (*) in the peaks is slightly shifted, which in-turn transforms disorder to ordered phase. For all the sintered samples, the Mg–O vibration bands were assigned and in good agreement with the literature data [49].

3.5 SEM and TEM analysis

Figure 5 shows the high resolution scanning electron microscopy (HR-SEM) images of sintered MgAl_2O_4 samples at room temperature. From the surface morphological images, it was observed that, the sintered samples show different surface morphological behavior due to sintering effect. The average grain size of samples was calculated 17 nm, 28 nm and 40 nm for Mg5, Mg7 and Mg9 samples, receptively. On increasing the sintering temperature, the grain size is increased and the grains are in irregular shape and size. The surface morphology of samples was slightly porous agglomerated and indistinguishable. The crystallite size and grain size are different because of the crystalline size measure from XRD (the unity variation of crystalline region that diffracted by X-ray coherently) and the grain sizes are measured over in a particular region of the sample through the visible grain boundaries [50]. To ascertain the particle size of the Mg5, Mg7 and Mg9 samples, TEM measurements were carried out at the room temperature and shown in Fig. 6. The images represent that Self-agglomerated its form a spherical shape. The average particle size was calculated from TEM images by using ImageJ software and it have been founded range between 24 nm for Mg5, 28 nm for Mg7 and 33 nm for Mg9. While increasing the calcined temperature as gradually as particle size also increases. The observed TEM results will be in good agreement with SEM analysis.

3.6 Electrical properties

The divergence in the dielectric properties mostly in the spinel aluminate systems depends on several factors like particle size [51], cation distribution [52] and doping effect [53], which are rarely reported in the literature. In this way in the present work, we report on the influence of the sintering effect on the dielectric properties particularly

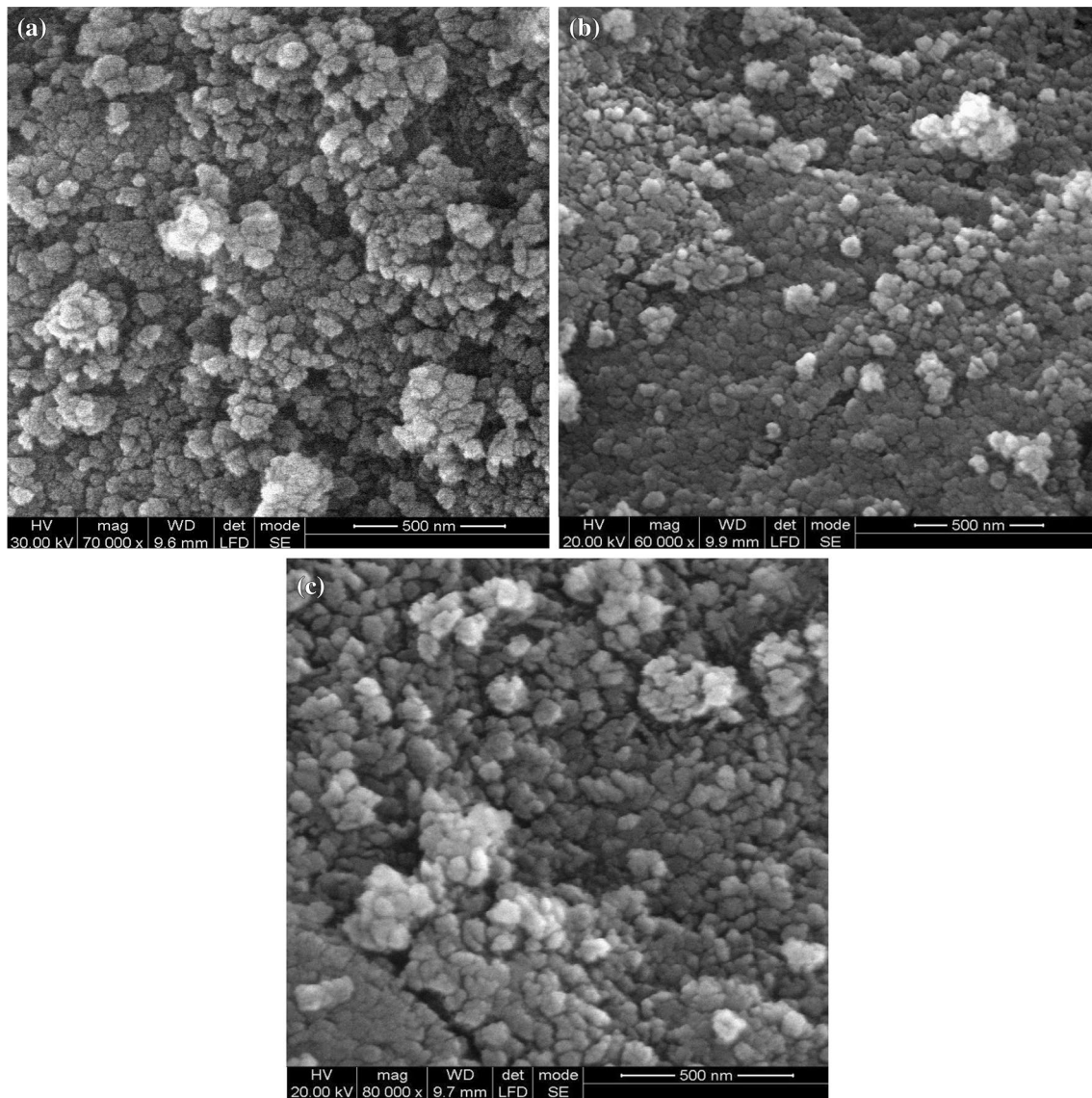


Fig. 5 SEM surface morphological images of MgAl_2O_4 samples sintered at different temperatures. **a** Mg5, **b** Mg7 and **c** Mg9

in the spinel aluminate system MgAl_2O_4 as below. For the prepared Mg5, Mg7 and Mg9 samples, the dielectric measurements were carried out in the frequency range from 1 Hz to 1 MHz at room temperature. The real part of permittivity (ϵ') value was calculated by using following equations.

$$\epsilon' = \frac{Cd}{A\epsilon_0} \quad (8)$$

where d is the thickness and A is the area of cross-section of the prepared pelletized samples. The ϵ_0 is permittivity of free space and C is the capacitance of prepared sample at a given frequency. The real part of dielectric constant value is increases at lower temperature and remaining constant at the high frequency region.

The frequency dispersion behavior of real part of dielectric constant and $\tan(\delta)$ were shown in Fig. 7a for Mg5, Mg7 and Mg9 samples. From Fig. 7a, we observed that as the sintering temperature increases, as usual the real part of dielectric constant also increases in the low frequency region. The real part shows a decreasing trend with respect to increasing frequency which can be clarified on the basis of Koop's phenomenological theory and the Maxwell Wagner interfacial polarization model [54]. The possible explanation for the increase in the value ϵ' at the lower frequency region was due to accumulation of charges within the grain or at the grain boundary region or due to the interfacial effect of electrode-sample. This may be expected to occur normally at the interfacial region and also due to space charge polarization of the sample.

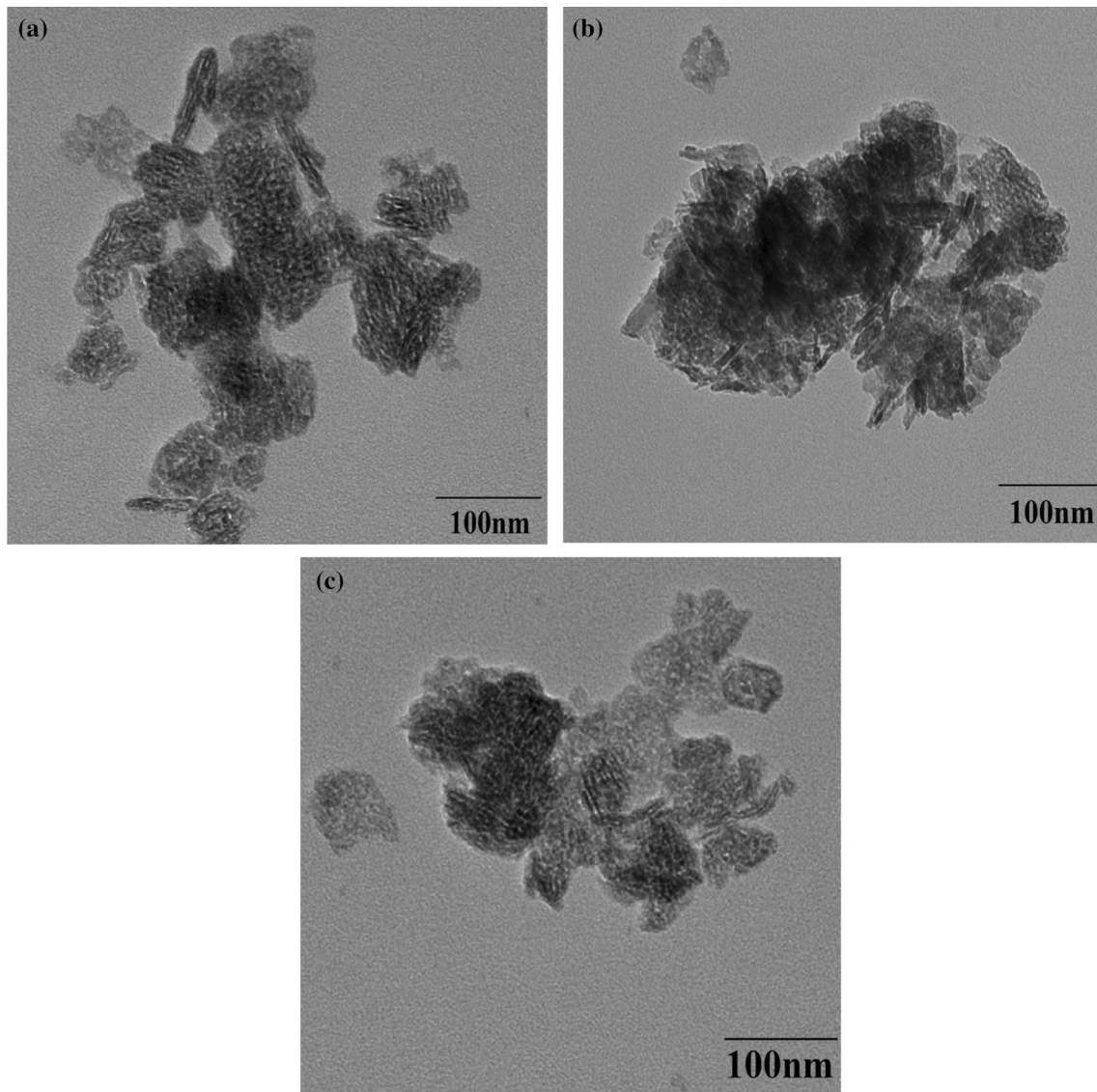


Fig. 6 TEM image of MgAl_2O_4 samples sintered at different temperatures. **a** Mg5, **b** Mg7 and **c** Mg9

However, the abnormal behavior as seen between 100 and 1000 Hz for 700 °C sintered sample (Mg7), which is clearly indicated in Fig. 7b and nearly a constant magnitude at the high frequency region. This can be explained as follows: the polarization mechanism is similar to the conduction process, as the hopping of electron exchange between Al^{2+} and Al^{3+} ion sites, which contributes to the polarization in the magnesium aluminate samples [53]. However, the $\tan \delta$ shows a relaxation peak shift as observed from Fig. 7c and also disorder phase plays an important role of abnormal shift was observed at 700 °C.

At the low frequency region, the electron follows as increasing the frequency of external field due to the decreasing polarization, where electron cannot follow the interchanging field. Therefore, the dielectric constant decreases

while increasing the particle size. In the present case, the dielectric loss $\tan \delta$ shows a dispersion behavior, which may be due to the space charge formation occur interlayer of air gap and its refer to an in-homogenies and exist of defects. The imaginary part of dielectric constant hence, the $\tan \delta$ shows an increasing trend with respected to applied frequency and also due to particle size behavior of sample. The relaxation peaks also shifted towards higher frequency end and the observed result suggested the presence of Debye-like dipolar relaxation in the material.

The Cole–Cole plot of real versus imaginary part of dielectric constant were shown in Fig. 8. A depressed semi-circle arc behavior was observed in the Cole–Cole plot for the Mg5 and Mg7 samples at room temperature. Ideally, two semi-circular arcs are obtained for the hetero-structure

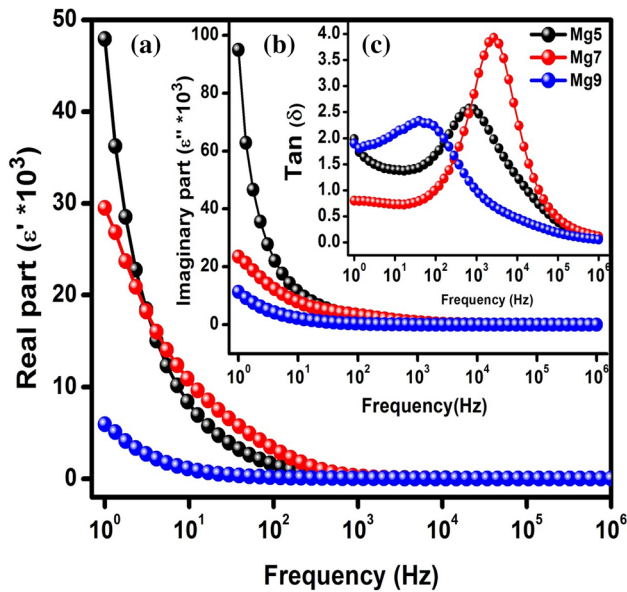


Fig. 7 Room temperature frequency dispersive behavior of (a) real and (b) imaginary parts of dielectric constant and (c) $\tan(\delta)$ for MgAl_2O_4 samples sintered at different temperature

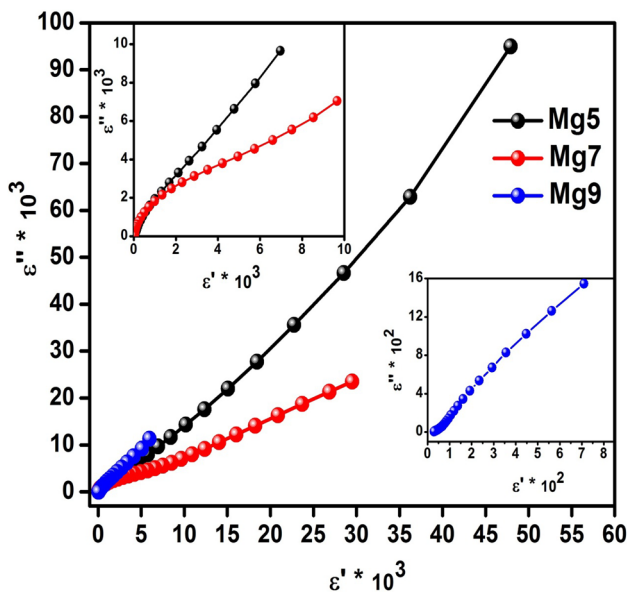


Fig. 8 Room temperature Cole–Cole plot dielectric constant for MgAl_2O_4 samples sintered at different temperatures

materials corresponding to the grains (sample) and electrode effect of samples which corresponds to the low and mid frequencies respectively [55].

4 Conclusions

The sintering effect of order–disorder phase transition for magnesium aluminate (MgAl_2O_4) was reported. The samples were synthesized by co-precipitation method. The prepared sample was sintered at different temperatures. The order–disorder phase transition of cubic spinel aluminate was confirmed by powder XRD at room temperature and UV-absorbance spectra. From optical band gap measurements, we observed that an increasing behavior due to sintering effect, and the band gap also increases, which were explained by Burstein–Moss shift with size dominating role of blue shift of MgAl_2O_4 . In addition, the cation site distributions of sintered samples and the effect of order–disorder phase transition and sintering effect were observed in solid-state nuclear magnetic resonance (SS-NMR) spectral analysis and the observe results are reported. The surface morphology of grain size for sintered samples was analyzed using HR-SEM. Also, the particle size of the sintered samples was calculated using TEM measurements. The calculated value of the particle sizes from SEM and TEM micrographs shows an increase in their magnitude with the sintering temperature, which may be due to agglomeration of the grains in the prepared samples. The stretching and bending mode of vibration band were also conferred the order–disorder phase transition in the sintered samples through Fourier transform infrared spectroscopic analysis. The frequency dispersion of real and imaginary parts of dielectric constant was measured and analyzed at room temperatures for phase evolution and sintering effect which perceive of MgAl_2O_4 . The observed results are reported.

Author contributions It has been approved by all of the authors, and due care has been taken to ensure the integrity of the manuscript.

Compliance with ethical standards

Conflict of interest The authors declare that they have no conflict of interest.

References

1. N.W. Grimes, The spinels: versatile materials. *Phys. Technol.* **6**, 22–27 (1975)
2. I. Ganesh, A review on magnesium aluminate (MgAl_2O_4) spinel: synthesis, processing and applications. *Int. Mater. Rev.* **58**(2), 63–112 (2013)
3. C. Baudin, R. Martinez, P. Pena, High-temperature mechanical behavior of stoichiometric magnesium spinel. *J. Am. Chem. Soc.* **78**(7), 1857–1862 (1995)
4. C.-F. Tseng, H.-H. Tung, C.-K. Hsu, C.-C. Yu, C.-H. Hsu, Dielectric characteristics of ($\text{Mg}_{1/2}\text{Zn}_{1/2}$) Al_2O_4 ceramics at microwave frequencies. *J. Alloys Compd.* **502**, 136–138 (2010)

5. J. Guo, H. Lou, H. Zhao, X. Wang, X. Zheng, Novel synthesis of high surface area MgAl_2O_4 spinel as catalyst support. *Mater. Lett.* **58**, 1920–1923 (2004)
6. O. Padmaraj, M. Venkateswarlu, N. Satyanarayana, Structural, electrical and dielectric properties of spinel type MgAl_2O_4 nanocrystalline ceramic particles synthesized by the gel-combustion method. *Ceram. Int.* **41**, 3178–3185 (2015)
7. A. Laobuthee, S. Wongkasemjit, E. Traversa, R.M. Laine, MgAl_2O_4 spinel powders from oxide one pot synthesis (OOPS) process for ceramic humidity sensors. *J. Eur. Ceram. Soc.* **20**, 91–97 (2000)
8. R. Maschio, B. Fabbri, C. Fiori, Industrial applications of refractories containing magnesium aluminate spinel. *Ind. Ceram.* **8**, 121–126 (1988)
9. M.A. Valenzuela, J.-P. Jacob, P. Bosch, S. Reijne, B. Zapata, H.H. Brongersma, The influence of the preparation method on the surface structure of ZnAl_2O_4 . *Appl. Catal. A* **148**, 315–324 (1997)
10. M.J. Iqbal, B. Ismail, Electric, dielectric and magnetic characteristics of Cr^{3+} , Mn^{3+} and Fe^{3+} substituted MgAl_2O_4 : effect of pH and annealing temperature. *J. Alloys Compd.* **472**, 434–440 (2009)
11. S. Tripathy, D. Bhattacharya, Rapid synthesis and characterization of mesoporous nano-crystalline MgAl_2O_4 via flash pyrolysis route. *J. Asian Ceram. Soc.* **1**, 328–332 (2013)
12. K. Zaharieva, M. Shopska, I. Yordanova, S. Damyanova, The effect of synthesis conditions on the physicochemical properties of magnesium aluminate materials. *Ceram. Int.* **44**, 326–332 (2018)
13. I. Ganesh, B. Srinivas, R. Johnson, B.P. Saha, Y.R. Mahajan, Microwave assisted solid state reaction synthesis of MgAl_2O_4 spinel powders. *J. Eur. Ceram. Soc.* **24**, 201–207 (2004)
14. P. Barpanda, S.K. Behera, P.K. Gupta, S.K. Pratihari, S. Bhattacharya, Chemically induced order disorder transition in magnesium aluminium spinel. *J. Eur. Ceram. Soc.* **26**, 2603–2609 (2006)
15. K.E. Sickafus, Comment on order–disorder phase transition induced by swift ions in MgAl_2O_4 and ZnAl_2O_4 spinels by D. Simeone et al. *J. Nucl. Mater.* **300**, 151–160 (2002). *J. Nucl. Mater.* **312**, 111–123 (2003)
16. D. Simeone, C. Dodane-Thiriet, D. Gosset, P. Daniel, M. Beauvy, Order–disorder phase transition induced by swift ions in MgAl_2O_4 and ZnAl_2O_4 spinels. *J. Nucl. Mater.* **300**, 151–160 (2002)
17. K.E. Sickafus, J.M. Wills, Structure of spinel. *J. Am. Ceram. Soc.* **82**(12), 3279–3292 (1999)
18. R.J. Hill, J.R. Craig, G.V. Gibbs, Systematics of the spinel structure type. *Phys. Chem. Miner.* **4**, 317–339 (1979)
19. S. Nishikawa, Structure of some crystals of spinel group. *Tokyo Sugaku-Buturiggakwai Kizi Dai 2 Ki* **5**(7), 199–209 (1915)
20. W.H. Bragg, The structure of the spinel group of crystals. *Philos. Mag.* **30**(176), 305–315 (1915)
21. H.-H. Ko, G. Yang, H.-Z. Cheng, M.-C. Wang, X. Zhao, Growth and optical properties of cerium dioxide nano-crystallites prepared by co-precipitation routes. *Ceram. Int.* **40**, 4055–4064 (2014)
22. G. Gusmano, P. Nunziante, E. Traversa, The mechanism of MgAl_2O_4 spinel formation from the thermal decomposition of co-precipitated hydroxides. *J. Eur. Ceram. Soc.* **7**, 31–39 (1991)
23. T. Yang, B. Zhang, Q. Zhao, D. He, P. Luo, A. Chang, Vacuum hot pressed highly dense, nano-grained $\text{Mg}(\text{Al}_{1-x}\text{Cr}_x)_2\text{O}_4$ ceramics. *Mater. Lett.* **194**, 42–44 (2017)
24. Y. Wen, X. Liu, X. Chen, Q. Jia, R. Yu, T. Ma, Effect of heat treatment conditions on the growth of MgAl_2O_4 nanoparticles obtained by sol-gel method. *Ceram. Int.* **43**, 15246–15253 (2017)
25. S. Takahashi, A. Kan, H. Ogawa, Microwave dielectric properties and crystal structures of spinel-structured MgAl_2O_4 ceramics synthesized by a molten-salt method. *J. Eur. Ceram. Soc.* **37**, 1001–1006 (2017)
26. L. Cornu, M. Gaudon, V. Jubera, ZnAl_2O_4 as potential sensor: variation of luminescence with thermal history. *J. Mater. Chem. C* **1**(34), 5419–5428 (2013)
27. V. Sreeja, T.S. Smitha, D. Nand, T.G. Ajithkumar, P.A. Joy, Size dependent coordination behavior and cation distribution in MgAl_2O_4 nanoparticles from ^{27}Al solid state NMR studies. *J. Phys. Chem. C* **112**, 14737–14744 (2008)
28. A.A. Da Silva, A. de Souza Goncalves, M.R. Davolos, Characterization of nano-sized ZnAl_2O_4 spinel synthesized by the sol–gel method. *J. Sol-Gel. Sci. Technol.* **49**, 101–105 (2009)
29. H.J. Jakobsen, J. Skibted, H. Bildsbe, N.C. Andniels, Magic-angle spinning NMR spectra of satellite transitions for quadrupolar nuclei in solids. *J. Magn. Reson.* **85**, 173–180 (1989)
30. L. Schreyeck, A. Wlosik, H. Fuzellier, Influence of the synthesis route on MgAl_2O_4 spinel properties. *J. Mater. Chem.* **11**, 483–486 (2001)
31. B.J. Wood, R.J. Kirkpatrick, B. Montez, Order-disorder phenomena in MgAl_2O_4 spinel. *Am. Mineral.* **71**, 999–1006 (1986)
32. H. Li, Y. Liu, J. Tang, Y. Deng, Synthesis, characterization and photo-catalytic properties of $\text{Mg}_{1-x}\text{Zn}_x\text{Al}_2\text{O}_4$ spinel nanoparticles. *Solid State Sci.* **58**, 14–21 (2016)
33. T.A. Bazilevskaya, V.T. Gritsyna, D.V. Orlinski, L.V. Udaloova, A.V. Voitsenya, The effect of composition, processing conditions, and irradiation, on lattice defects in spinel ceramics. *J. Nucl. Mater.* **253**, 133–140 (1998)
34. V. Piriyaowong, V. Thongpool, P. Asanithi, P. Limsuwan, Preparation and characterization of alumina nanoparticles ionized water using laser ablation technique. *J. Nanomater.* (2012). <https://doi.org/10.1155/2012/819403>
35. X. Qian, B. Li, H. Mu, J. Ren, Y. Liu, Y. Ha, F. Li, Deep insight into the photo-catalytic activity and electronic structure of amorphous earth-abundant MgAl_2O_4 . *Inorg. Chem. Front.* **4**, 1832–1840 (2017)
36. K. Kanwal, B. Iamail, K.S. Rajani, N.J. Suthan Kissinger, A. Zeb, Effect of Co^{2+} ions doping on the structural and optical properties of magnesium aluminate. *J. Electron. Mater.* **46**(7), 4206–4213 (2017)
37. M.A. Monge, A.I. Popov, C. Ballesteros, R. Gonzalez, Formation of anion-vacancy clusters and nano-cavities in thermo chemically reduced MgO single crystals. *Phys. Rev. B* **62**(14), 9299–9304 (2000)
38. J.I. Pankove, *Optical Process in Semiconductor* (Dover publications, Inc., New York, 1971)
39. S. Joshi, M. Kumar, S. Chhoker, G. Srivastava, M. Jewariya, V.N. Singh, Structural, magnetic, dielectric and optical properties of nickel ferrite nanoparticles synthesized by co-precipitation method. *J. Mol. Struct.* **1076**, 55–62 (2014)
40. M. Fox, *Optical Properties of Solids*. (Oxford University press, Oxford, 2001)
41. H. Guo, J. Chen, W. Weng, Q. Wang, S. Li, Facile template-free one-pot fabrication of ZnCo_2O_4 microspheres with enhanced photocatalytic activities under visible-light illumination. *Chem. Eng. J.* **239**, 192–199 (2014)
42. M.Y. Nassar, I.S. Ahmed, I. Samir, A novel synthetic route for magnesium aluminate (MgAl_2O_4) nanoparticles using sol–gel auto combustion method and their photo-catalytic properties. *Spectrochim. Acta, Part A* **131**, 329–334 (2014)
43. J. Preudhommei, P. Taiwe, Infra-red studies of spinels-III. The normal II-III spinel. *Spectrochim. Acta* **27A**, 1817–1822 (1970)
44. J. Preudhommei, P. Tarte, Infrared studies of spinel-I: a critical discussion of the actual interpretations. *Spectrochim. Acta* **27A**, 961–968 (1970)
45. Siby Kurien, Structural and electrical properties of certain nanocrystalline aluminates, e-Thesis
46. A. Nag, T.R.N. Kutty, Role of B_2O_3 on the phase stability and long phosphorescence of SrAl_2O_4 : Eu, Dy. *J. Alloys Compd.* **354**, 221–231 (2003)
47. M.I. Baraton, P. Quintard, Infra-red evidence of order-disorder phase transition in Al_2O_3 . *J. Mol. Struct.* **79**, 337–340 (1982)

48. P. Fu, W. Lu, W. Lei, K. Wu, Y. Xu, J. Wu, Thermal stability and microstructure characterization of MgAl_2O_4 nanoparticles synthesized by reverse micro-emulsion method. *Mater. Res.* **16**(4), 844–849 (2013)
49. L.-Z. Pei, W.-Y. Yin, J.-F. Wan, J. Chen, C.-G. Fan, Q.-F. Zhang, Low temperature synthesis of magnesium oxide and spinel powders by a sol-gel process. *Mater. Res.* **13**(3), 339–343 (2010)
50. S. Bandyopadhyay, G.K. Paul, R. Roy, S.K. Sen, S. Sen, Study of structural and electrical properties of grain-boundary modified ZnO films prepared by sol-gel technique. *Mater. Chem. Phys.* **74**, 83–91 (2002)
51. S. Kurien, J. Mathew, S. Sebastian, S.N. Potty, K.C. George, Dielectric behavior and ac electrical conductivity of nanocrystalline nickel aluminate. *Mater. Chem. Phys.* **98**, 470–476 (2006)
52. S. Kurien, J. Mathew, S. Sebastian, K.C. George, Structural and electrical properties of nano-sized magnesium aluminate. *Indian J. Pure Appl. Phys.* **42**, 926–933 (2004)
53. R. Samkaria, V. Sharma, Structural, dielectric and electrical studies of $\text{MgAl}_{2-2x}\text{Y}_{2x}\text{O}_4$ ($x = 0.00\text{--}0.05$) cubic spinel nano aluminate. *J. Electroceram.* **31**, 67–74 (2013)
54. C.G. Koops, On the dispersion of resistivity and dielectric constant of some semiconductors at audio frequencies. *Phys. Rev.* **83**, 121 (1951)
55. T. Hussain, M. Junaid, S. Atiq, S.K. Abbas, S.M. Ramay, B.F. Alrayes, S. Naseem, Tunable dielectric behaviour and energy band gap range of ZnAl_2O_4 ceramics mediated by Mg substitution. *J. Alloys Compd.* **724**, 940–950 (2017)